

Evidence for a hot galactic halo around the Andromeda Galaxy using fast radio bursts along two sightlines.

RESHMA ANNA-THOMAS ^{1,2,3,4} CASEY J. LAW ^{5,6} ERIC W. KOCH ⁷ ALEXA C. GORDON ⁸ KRITTI SHARMA ^{5,6}
BENJAMIN F. WILLIAMS ⁹ NICKOLAS M. PINGEL ¹⁰ SARAH BURKE-SPOLAOR ^{1,2,11} ZHUO CHEN ⁹
JORDAN STANLEY^{1,2} CALVIN DEAR^{1,2} FRANK VERDI^{5,6} J. XAVIER PROCHASKA ^{12,13,14} GEOFFREY C. BOWER ^{15,16}
LAURA CHOMIUK¹⁷ LIAM CONNOR ⁷ PAUL B. DEMOREST ¹⁸ WEN-FAI FONG ⁸ ANYA NUGENT ^{8,7} AND
FABIAN WALTER ¹⁹

¹West Virginia University, Department of Physics and Astronomy, P. O. Box 6315, Morgantown, WV, USA

²Center for Gravitational Waves and Cosmology, West Virginia University, Chestnut Ridge Research Building, Morgantown, WV, USA

³ASTRON, Netherlands Institute for Radio Astronomy, Oude Hoogeveensedijk 4, 7991 PD Dwingeloo, The Netherlands

⁴Anton Pannekoek Institute for Astronomy, University of Amsterdam, Science Park 904, 1098 XH Amsterdam, The Netherlands

⁵Cahill Center for Astronomy and Astrophysics, MC 249-17 California Institute of Technology, Pasadena CA 91125, USA

⁶Owens Valley Radio Observatory, California Institute of Technology, Big Pine CA 93513, USA

⁷Center for Astrophysics | Harvard & Smithsonian, 60 Garden St., 02138 Cambridge, MA, USA

⁸Center for Interdisciplinary Exploration and Research in Astrophysics (CIERA) and Department of Physics and Astronomy, Northwestern University, Evanston, IL 60208, USA

⁹Astronomy Department, University of Washington, Seattle, WA, 98195

¹⁰University of Wisconsin–Madison, Department of Astronomy, 475 N Charter St, Madison, WI 53703, USA

¹¹Sloan Fellow

¹²Department of Astronomy and Astrophysics, University of California, Santa Cruz, CA 95064, USA

¹³Kavli Institute for the Physics and Mathematics of the Universe, 5-1-5 Kashiwanoha, Kashiwa 277-8583, Japan

¹⁴Division of Science, National Astronomical Observatory of Japan, 2-21-1 Osawa, Mitaka, Tokyo 181-8588, Japan

¹⁵Academia Sinica Institute of Astronomy and Astrophysics, 645 N. A'ohoku Pl., Hilo, HI 96720, USA

¹⁶Department of Physics and Astronomy, University of Hawaii at Manoa, 2505 Correa Road, Honolulu, HI 96822, USA

¹⁷Center for Data Intensive and Time Domain Astronomy, Department of Physics and Astronomy, Michigan State University, East Lansing, MI 48824, USA

¹⁸National Radio Astronomy Observatory, P.O. Box O, Socorro, NM 87801, USA

¹⁹Max Planck Institut für Astronomie, Königstuhl 17, D-69117, Heidelberg, Germany

ABSTRACT

Fast Radio Bursts (FRBs) are millisecond-duration radio transients that serve as unique probes of ionized extragalactic matter. We report the discovery and localization of two FRBs piercing the Andromeda Galaxy (M31) with the *realfast* transient-detection system at the Very Large Array. These unique sightlines enable constraints on M31's electron density distribution. We localized FRB 20230930A to a host galaxy at redshift $z = 0.0925$ and FRB 20230506C to a host galaxy at redshift $z = 0.3896$. After accounting for the dispersion contributions from the Milky Way, the host galaxies, and the intergalactic medium, we estimate M31's contribution to be 26–239 pc cm⁻³ toward FRB 20230930A and 51–366 pc cm⁻³ toward FRB 20230506C, within the 90% credible interval (CI). By modeling the M31 disk's contribution, we isolate the halo component and find that M31's halo contributes 7–169 pc cm⁻³ along FRB 20230930A (90% CI). The inferred values of DM_{M31,halo} from the FRBs are consistent with predictions from a modified Navarro–Frenk–White (mNFW) profile at the corresponding impact parameter. The cool and warm phase gas is unlikely to account for the DM_{M31,halo} unless the ionization fraction is as high as 90%. While limited to two sightlines, these results offer tentative evidence for the existence of a hot halo surrounding M31. We also discuss the potential contribution of other foreground structures, particularly in explaining the DM excess ob-

served in FRB 20230506C. This work demonstrates how FRBs can be used to probe the circumgalactic medium of intervening galaxies.

Keywords: Radio transient sources (2008) — Radio Bursts(1339) — Galaxies(573)

1. INTRODUCTION

A hot corona around our Galaxy was first predicted by Spitzer (1956) as the cause of absorption lines in the spectra of stars at high Galactic latitude. The exploration of this circumgalactic gas was then carried out by absorption line spectroscopy of bright background sources. The circumgalactic medium (CGM) regulates the inflow and outflow of gases and therefore plays an important role in galaxy evolution. The CGM represents a multiphase metal-enriched gas reservoir around all galaxies and likely extends beyond the virial radius, R_{vir} (e.g. Tumlinson et al. 2017). Apart from absorption line studies, independent constraints on the CGM were measured in the microwave regime by studying the distortion in the cosmic microwave background spectrum by the hot electrons in the halo. This process termed as the thermal Sunyaev-Zeldovich (SZ) effect (Sunyaev & Zeldovich 1980), has been used to study the CGM of nearby galaxies (Bregman et al. 2022). X-ray emission due to thermal bremsstrahlung (Li et al. 2018) has also been used to study the hot CGM around nearby galaxies.

The Andromeda galaxy (M31), at a distance of 761 ± 11 kpc (Li et al. 2021), is the closest large galaxy to the Milky Way and its halo subtends an angle of 30° in the sky, making it a perfect candidate to study the CGM. Lehner et al. (2015) discovered evidence of a massive extended CGM around M31 using far-ultraviolet absorption lines of metal ions corresponding to a cold phase ($T \leq 10^4$ K) and a warm phase ($T \sim 10^{5.5}$ K). They showed that this CGM is bound, exists in multiple phases, and its ionization fraction increases with the radius from the center. The baryon mass within R_{vir} for the cold-warm phase ($T \sim 10^4 - 10^{5.5}$ K) CGM was estimated to be $> 4 \times 10^{10} (Z/0.3Z_\odot)^{-1} M_\odot$ (Lehner et al. 2020), where Z denotes the metallicity of the medium. Observational evidence of the hot ($T \geq 10^6$ K) phase of the CGM, presumably surrounding the cold phase, is still lacking.

The frequency-dependent dispersion associated with fast radio bursts (FRBs; Lorimer et al. (2007)) provides a unique probe to measure the baryon content of the intervening medium between the source and the observer. The dispersion measure, $\text{DM} = \int_d n_e dl$ is a direct measurement of the electron density in the observer’s line of sight. Previous studies have used FRBs to measure

the electron density of the halos of intervening galaxies (Prochaska et al. 2019; Wu & McQuinn 2023), including the Milky Way (Ravi et al. 2023; Cook et al. 2023), the intracluster medium (Connor et al. 2023), and the intergalactic medium (Macquart et al. 2020). Previously, Connor et al. (2020); van Leeuwen et al. (2023) detected FRBs skewering the M31-M33 halos and suggested that the shared plasma of the group contributed to the DM of the FRB. In a different study using hundreds of FRBs detected by the Canadian Hydrogen Intensity Mapping Experiment (CHIME), Connor & Ravi (2022) finds weak evidence for DM excess contributed by the halos of M31 and M33, whereas Wu & McQuinn (2023) found the evidence to be only marginal. Therefore, it is crucial to detect more FRBs intersecting the local group galaxies to reliably understand the CGM around these galaxies and its potential impact on FRB detection.

realfast (Law et al. 2015, 2018) is a real-time cosmological transient search, detection, and localization system operating at the Karl J. Jansky Very Large Array (VLA) between the frequencies 1 to 10 GHz. *realfast* has been instrumental in the localization of many FRBs like the first repeating FRB 20121102A (Chatterjee et al. 2017), FRB 20180916B (Aggarwal et al. 2020) and FRB 20190520B (Niu et al. 2022). It has also discovered FRB 20190614D (Law et al. 2020) and a Galactic pulsar-like source J1818–1531 (Anna-Thomas et al. 2024). In this paper, we discuss the discovery and localization of two FRBs by *realfast* that pierce through M31.

This paper is organized into multiple sections: §2 describes radio and optical observations and data reduction, §3 discusses the DM budget and constraints the DM contribution from M31, §4 discusses various DM contributions, and §5 summarizes the results. Throughout this paper, we adopt cosmological model and parameters from the Planck 2018 analysis for any calculation that requires assumed cosmology Planck Collaboration et al. (2020).

2. OBSERVATIONS AND DATA REDUCTION

2.1. VLA/Realfast observation

The VLA was observing the Local Group Legacy survey (EVLA 20A-346; P.I. Adam Leroy) which targets deep, high spatial resolution imaging of 21 cm and L-Band continuum emission of six local group galaxies, including M31. The *realfast* transient-detection sys-

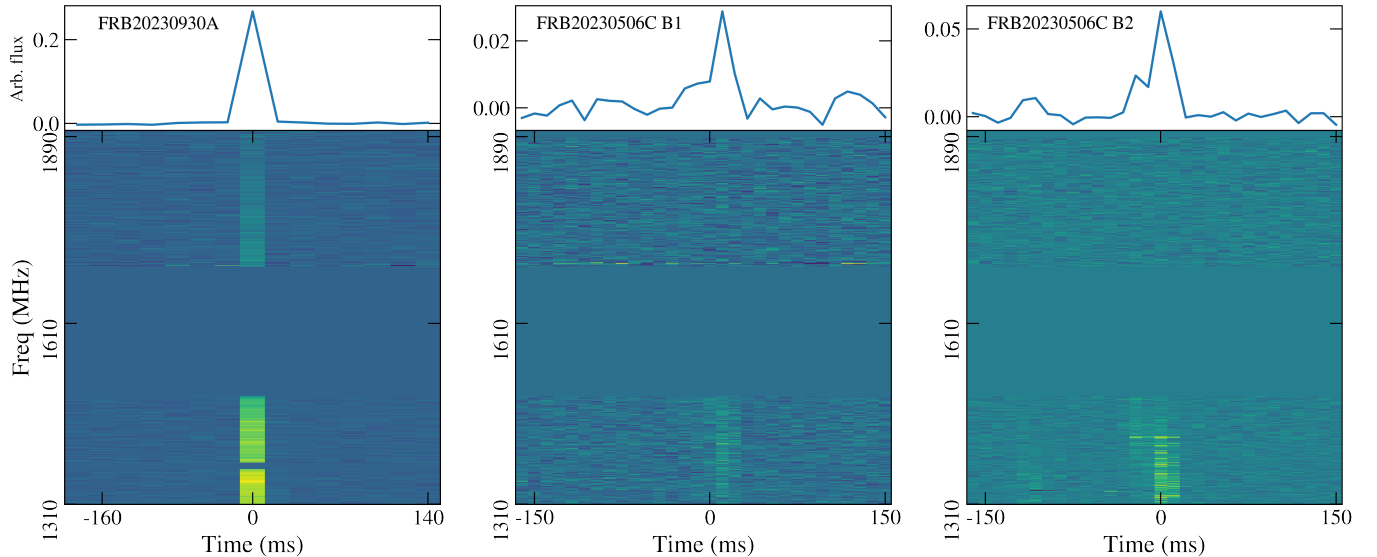


Figure 1. Dynamic spectrogram (bottom) and frequency-averaged time profile (top) of the *realfast* bursts, dedispersed at their detection DM. The data have 10 ms time resolution and 1 MHz frequency resolution; note that channels between 1490 MHz and 1690 MHz were not recorded by the *realfast* system

tem ran commensally with these observations, ingesting correlated voltages sampled at 10 ms resolution. The software RFPPIPE applies online calibration, searches for bursts at many different trial DM and widths. Candidates above 8σ fluence limit for a 10 ms image (0.29 Jy ms at L-band) triggered the recording of a few seconds of visibility data centered around the candidate. These candidates are then visually inspected by the *realfast* users.

On May 6, 2023 (MJD 60070) and on September 30, 2023 (MJD 60217), *realfast* detected two FRBs, FRB 20230930A and FRB 20230506C, when the telescope was pointed at J2000 RA = 00h41m40.844s, DEC = $41^\circ 44' 02.379''$ (field=M31LARGE_47) and RA = 00h48m42.535s, DEC = $42^\circ 00' 51.122''$ (M31LARGE_4), respectively. This triggered the download of 10-ms Science Data Model (SDM) data. Repeat bursts from FRB 20230506C were subsequently detected on August 26, 2023 (MJD 60182) and September 28, 2023 (MJD 60215). The VLA was in the B configuration on 60070, and in A configuration on 60182, 60215, and 60217. The frequency range of the *realfast* data is 1.308 – 2.012 GHz and is divided into 8 spectral windows, each having 64 channels with 1 MHz resolution. We also note that the frequencies between 1.49 – 1.69 GHz were not recorded due to the spectral set up of the primary observation. The *realfast* system also did not store the visibilities on MJD 60182 for FRB 20230506C and it was only detected by the realtime pipeline. For both fields, we observed the sources J2355+4950 for phase calibration at regular intervals, 3C48 for flux calibra-

tion and J1800+7828 for polarization calibration at the end of each track.

The burst profiles and spectrograms are shown in Figure 1. We used the package BURSTFIT on the *realfast* bursts to do spectro-temporal modeling of the bursts. We modeled the temporal profile of the burst using a Gaussian convolved with an exponential tail and the time-averaged spectra of the burst using a simple Gaussian as done in Aggarwal et al. (2021). We do not report the scattering timescale (τ) since the ratio of $\tau/\sigma_t < 3$, which indicates that the scattering is not significant. Here σ_t represents the standard deviation of the Gaussian pulse. Using this modeling, we fit for the width, DM, center frequency and the bandwidths of each bursts.

The S/N maximized DM of FRB 20230930A is $456^{+0.5}_{-0.6}$ pc cm $^{-3}$ and the DM of the brightest burst of FRB 20230506C is 772^{+3}_{-2} pc cm $^{-3}$. The burst properties of the three *realfast* bursts are given in Table 1.

2.2. *Realfast* imaging and localization

The real-time images of the candidates are convolved with the point spread function, and are made with several assumptions like coarse DM grid, non-optimal image size, simpler calibration model, etc. To rectify this, we followed the steps in Anna-Thomas et al. (2024) for post processing and offline imaging of the *realfast* data. An additional step of spectral-window mapping was applied to ensure that solutions were applied to the correct frequencies. As mentioned earlier, *realfast* did not record the fast-sampled visibility data for the FRB detected on MJD 60182. For the other

Properties	FRB 20230930A	FRB 20230506C B1	FRB 20230506C B2
RA	00h42m01.734s	00h48m23.9579s	00h48m23.9608s
Δ RA	0.1''	0.12''	0.12''
DEC	+41°25'02.4143''	+42°00'21.8822''	+42°00'21.9249''
Δ Dec	0.18''	0.18''	0.18''
S/N	55	14	38
MJD	60217.2074113	60070.7238837	60215.2046195
DM (pc cm ⁻³)	456 ^{+0.5} _{-0.6}	761 ⁺⁵ ₋₅	772 ⁺³ ₋₂
Flux (Jy)	0.27 ± 0.004	0.05 ± 0.001	0.14 ± 0.002
Width (ms)	8.7 ^{+1.1} _{-1.1}	18 ^{+1.4} _{-1.1}	17 ^{0.7} _{-0.7}
μ_f (MHz)	1329 ⁺¹⁰ ₋₁₀	1392 ⁺⁵ ₋₅	1351 ⁺³ ₋₃
σ_f (MHz)	134 ⁺⁷ ₋₇	59 ⁺⁶ ₋₅	58 ⁺³ ₋₃

Table 1. Observed properties of all *realfast* bursts.

S/N is the image plane signal-to-noise obtained during the offline refinement of the bursts.

MJD is the time of arrival of the bursts corrected to the barycentric frame of reference (TDB) and infinite frequency.

DM is the S/N maximizing dispersion measure obtained from BURSTFIT.

Flux as obtained from CASA’s *imfit*.

Width of the burst in ms as obtained from BURSTFIT.

μ_f is the center frequency of the burst obtained from BURSTFIT.

σ_f is the bandwidth of the burst spectra from BURSTFIT.

NOTE: *realfast* did not record the data for a burst of FRB 20230506C on MJD 60182 and hence it is omitted here.

three bursts, we created cleaned images using CASA and fitted the bursts by a 2D elliptical Gaussian using *imfit* to get the flux density, centroid position, and 1σ image-plane uncertainties. The statistical uncertainty in the position of FRB 20230930A is Δ RA_{stat} = 0.01'', Δ Dec_{stat} = 0.01'' and for FRB 20230506C is Δ RA_{stat} = 0.01'', Δ Dec_{stat} = 0.007''.

To determine the systematic offsets in the burst positions, we made a deep image of the VLA pointing of the fields of FRB 20230930A and FRB 20230506C. For the FRB 20230506C, we used the scan on the MJD of its brightest burst (B2). We ran a source extraction software PYBDSF (Mohan & Rafferty 2015) and identified 75 radio sources in the field. We then selected only the bright, compact sources using the criteria: 1) The peak intensity per beam of the source (in Jy/beam) should be 0.7 times greater than the total integrated flux density of the source (in Jy) in 1.5 GHz images, 2) the S/N of the source (ratio of peak intensity and the root-mean-square of the background) should be greater than 5. We were left with 27 sources in the fields of both FRBs. We cross-matched the positions of these radio sources with optical PAN-STARRS DR2 catalog, which is referenced to GAIA2 astrometric reference frame. We then subtracted the coordinates of the radio sources from the matched coordinates of the optical counterparts. We averaged the offset to determine a systematic relative offset Δ RA_{sys} = 0.10'', Δ Dec_{sys} = 0.18'' for FRB 20230930A and Δ RA_{sys} = 0.12'', Δ Dec_{sys} = 0.18'' for FRB 20230506C.

The full positional error is taken as the quadrature sum of the statistical and the systematic errors. The burst position of FRB 20230930A is J2000 RA = 00h42m01.734s and Dec = +41°25'02.4143'' and Δ RA = 0.10'' and Δ Dec = 0.18''. For FRB 20230506C, the burst position is J2000 RA = 00h48m23.9608s and Dec = +42°00'21.9249'' and Δ RA = 0.12'' and Δ Dec = 0.18''. The localization of the bursts is shown in Figure 2.

2.3. Follow-up GBT observation

Follow-up observations of the repeating FRB 20230506C were done using the 100-m Robert C. Byrd Green Bank Telescope (GBT) on MJDs 60360, 60363, 60367, 60368, 60371, 60373, 60374, and 60422. The VEGAS pulsar mode backend recorded the data in 8-bit PSRFITS format. The data has a center frequency of 1.4 GHz, bandwidth of 800 MHz, time resolution of 81.92 μ s and a frequency resolution of 195 kHz (4096 channels). Full polarization data were recorded in Stokes IQUV format. Bright quasars B2209+080 (only on MJD 60360) and 3C48 (on MJDs 60363 and 60371) were observed as flux calibrators and test pulsars B0531+21 and B1933+16 (only on MJD 60363) were observed for verifying calibration.

We cleaned the data to remove any radio frequency interference (RFI) using a custom filter that uses Savitzky-Golay and Spectral Kurtosis (Nita & Gary 2010) filter. We searched the GBT data using YOUR (Aggarwal et al. 2020) package which uses HEIMDALL (Barsdell 2012) to perform a single pulse search. We searched the data at different trial DMs between 600 – 900 pc cm⁻³. The

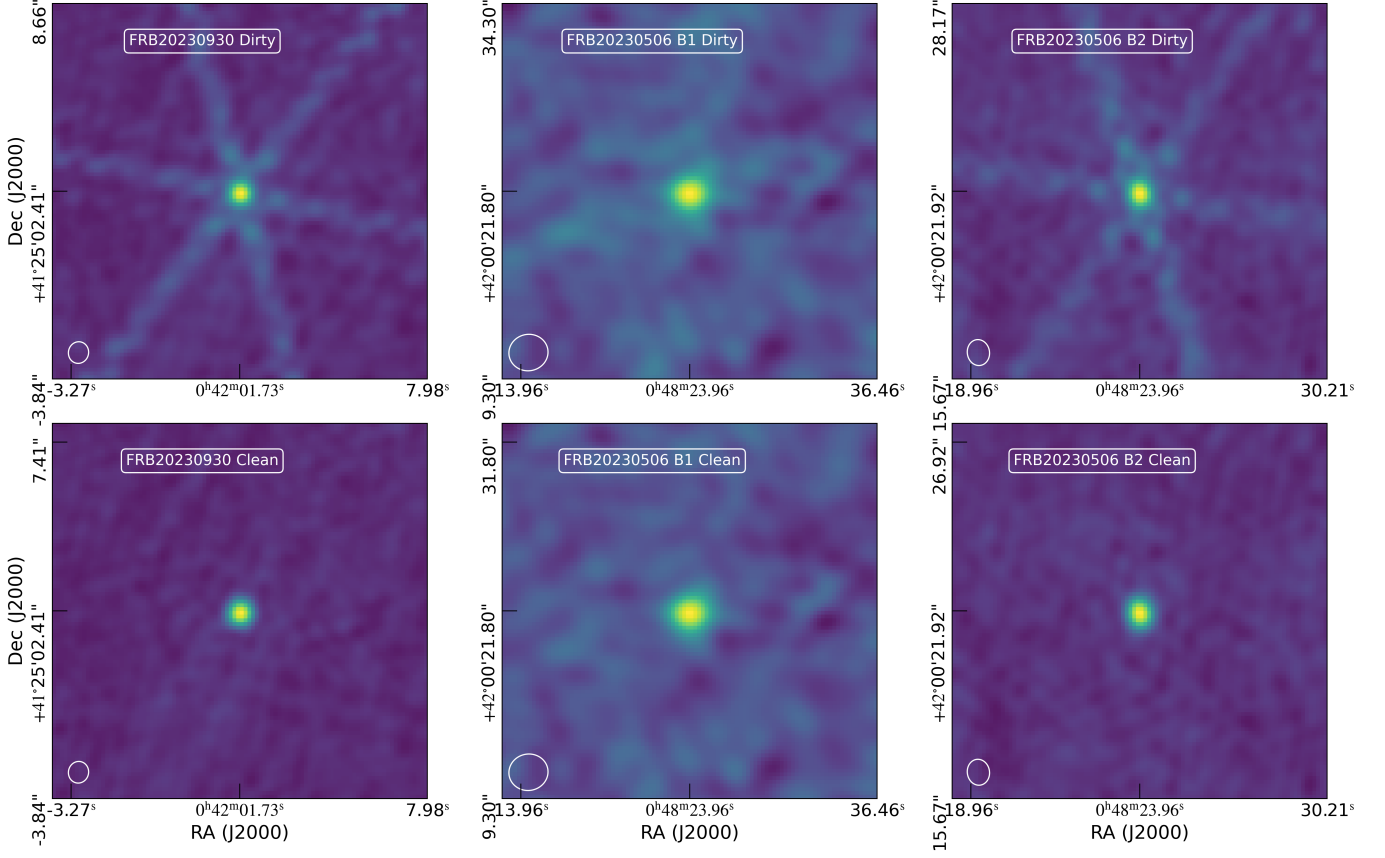


Figure 2. The dirty and clean maps of the *realfast* localization of the bursts. FRB 20230930A and FRB 20230506C B2 were observed in VLA A-configuration, and the FRB 20230506C B1 was observed in VLA B-configuration.

HEIMDALL candidates were then classified into real and RFI signals using the machine learning classifier FETCH (Agarwal et al. 2020).

We did not detect any bursts in a total of 5.7 hours on source above 7σ . From the *realfast* detection, we calculate the FRB burst rate to be 0.16 hr^{-1} above a flux limit of 29 mJy. The non-detection with GBT is therefore consistent with the burst rate of the FRB, assuming a Poissonian distribution.

2.4. VLA observation of M31

We also use the primary data output of 20A-346 from the Local Group L-band Survey (LGLBS; E. Koch et al., submitted) to check for detections of the host galaxies in the radio-continuum and 21-cm H I emission, and to place limits on the H I column density in these sightlines through M31. We use 43 M31 tracks from 20A-346, all taken in the VLA's B configuration¹. Each track includes a single 4 min scan on each of the 49

pointings in the complete LGLBS M31 mosaic. Here we only use field M31LARGE_14, which is closest to the FRB 20230930A location, and M31LARGE_47, which is closest to the FRB 20230506C location. After accounting for lost observing time due to RFI and antenna slewing, the total on-source integration was approximately 2.75 hr. We combine all tracks and image the source within 1.3–1.5 GHz from the L-band coverage, where there is minimal RFI at the VLA site, using `tclean` with robust-0.5 weighting and the `wproject` gridded.

For the FRB 20230930A (field M31LARGE_14), the continuum image is dynamic range limited using standard calibration techniques due to a 0.28 Jy/beam source that is $\approx 5'$ offset from the host location. We derived phase and amplitude self-calibration solutions using the `auto-selfcal`² routines. After self-calibration, the local RMS near the host location is $18 \mu\text{Jy/beam}$, roughly twice the theoretical noise limit of $10 \mu\text{Jy/beam}$. We use the self-calibrated image deconvolved to $3\sigma \approx 60 \mu\text{Jy/beam}$ with a restored beam size of $5'' \times 4''$.

¹ Additional A and B configuration observations are included in LGLBS, but calibration and quality assurance for these data remain on-going.

² github.com/jjtobin/auto_selfcal

We detect a $250 \pm 71 \mu\text{Jy}/\text{beam}$ L-band radio continuum source consistent with the host location. We fit the radio source to a 2D Gaussian using CARTA and find it is moderately resolved with a size of $7.1'' \times 5.4''$ with uncertainties of $\sim 1''$ in each direction, consistent with the pixel size of the map.

We image individual 1MHz ($\sim 50\text{km s}^{-1}$) channels after subtracting the continuum model. Using a $6''$ diameter circular aperture centered at the radio source location, we extract a spectrum from 1.32 to 1.404 GHz, corresponding to redshifts up to $z = 0.08$. Lower frequencies, approaching the optical line-determined redshift of $z = 0.0925$ (§2.5), are severely affected by RFI. The non-detection of HI up to $z = 0.08$ is therefore consistent with the host redshift of $z = 0.0925$ (§2.5).

Finally, we measure M31’s H I column density towards FRB 20230930A using LGLBS’s 0.4 km s^{-1} resolution coverage of the 21-cm H I line from -700 – 100 km s^{-1} (centered at M31’s systemic velocity near -300 km s^{-1}). We center an aperture corresponding to the synthesized beam size of $5.23 \times 4.81''$ and beam position angle of -76.8 deg on the location of the FRB in the integrated intensity image and extract a mean integrated intensity of 574 K km s^{-1} , corresponding to an H I column density of $1.05 \times 10^{21} \text{ cm}^{-2}$ under the optically thin assumption.

For the FRB 20230506C (field M31LARGE_47), we do not detect a radio continuum source and set a 5σ upper limit of $50 \mu\text{Jy}/\text{beam}$. The locally-measured rms of $10 \mu\text{Jy}/\text{beam}$ is consistent with the expected theoretical noise, and thus we did not use self-calibration for the continuum imaging. We estimate a H I column density of $1.7 \times 10^{21} \text{ cm}^{-2}$ towards the sightline of FRB 20230506C, measured by taking the mean pixel value in an integrated intensity image within an aperture matching the size of the synthesized beam ($5.1'' \times 4.8''$) that is centered on the sightline. We then integrated over velocity range of -700 km/s to $+100 \text{ km/s}$ LSR. The 1σ rms in the H I column density over this velocity range, for both the FRB lines-of-sight, is equal to $2.2 \times 10^{20} \text{ cm}^{-2}$.

2.5. Host Galaxy Optical Observations

To accurately determine the DM contribution from the intergalactic medium, it is necessary to obtain redshifts for the FRB host galaxies. Host galaxy observations also help us understand the progenitors of FRBs and their formation channels (Bhandari et al. 2022; Gordon et al. 2023; Law et al. 2024; Sharma et al. 2024; Shannon et al. 2024; Bhardwaj et al. 2024). In this subsection, we describe the optical identification and

follow-up of the host galaxies of FRB 20230930A and FRB 20230506C.

2.5.1. Host Galaxy of FRB 20230930A

We associate the FRB 20230930A with the galaxy coincident with the FRB location, a spiral galaxy at R.A. = $00\text{h}42\text{m}01.676\text{s}$, Dec = $41^\circ25'3.143''$, cataloged as WISEA J004201.69+412502.9 in the NASA Extragalactic Database and PSO J010.5070+41.4175 in the Pan-STARRS catalog. We employed ASTROPATH (Aggarwal et al. 2021) to determine the association probability of the FRB and host galaxy. We find that this galaxy has a posterior of 0.9994 adopting standard priors for the offset distribution of FRBs (Shannon et al. 2024), thus confirming the association. This galaxy was also detected in the archival Hubble Space Telescope (HST) data. The HST/ACS image was CR-cleaned, Gaia-aligned, and the calibrated drizzled images in the optical photometric bands F555W and F814W is shown in Figure 3. The Milky Way Galactic extinction along this sightline is $E(B - V) = 0.086$ mag. We use the PS1 r -band images to subtract stellar confusion and estimate a galaxy magnitude of $r = 18.706 \pm 0.065$ mag (corrected for Galactic dust-extinction).

Since PSO J010.5070+41.4175 lacks an archival spectrum, we followed it up with the Double Spectrograph (DBSP; Oke & Gunn 1982) mounted on the 200-inch Hale Telescope at the Palomar Observatory. The spectrum was obtained as a $1''$ single-slit observation on June 09, 2024 UTC with an average seeing of $1.6''$ during the observations. The 2D-spectrum shows a clear velocity gradient along the slit. The data were reduced using the DBSP_DRP (Mandigo-Stoba et al. 2022) software (built on top of the PyPEIT software package; Prochaska et al. 2020) and flux calibrated using the observations of a standard star obtained on the same night of observations. We measure the spectroscopic redshift of this galaxy using the Penalized PiXel-Fitting software (pPXF Cappellari 2022, 2017), where we jointly fit the stellar continuum and nebular emission using the MILES stellar library (Sánchez-Blázquez et al. 2006). We fit the $\text{H}\alpha$ complex to measure a redshift of $z = 0.0925 \pm 0.0002$. The Galactic extinction corrected $\text{H}\alpha$ flux is $1.16 \times 10^{-15} \text{ erg s}^{-1} \text{ cm}^{-2}$. We use Osterbrock & Ferland (2006) to estimate a star formation rate (SFR) from the $\text{H}\alpha$ luminosity, which is shown in Table 2.

To estimate the stellar mass, we used the PS1 r -band image to estimate that there is 1.7 magnitudes of stellar foreground confusion toward the host galaxy. We subtract this term from the PS1 cataloged $griz$ photometry and use the kcorrect Monte Carlo sampling of the

photometric errors to estimate a mean stellar mass of $9.1_{-1.6}^{+1.0} \times 10^9 M_{\odot}$.

2.5.2. FRB 20230506C

We obtained imaging of the field of FRB 20230506C on September 5, 2023 UTC, using Deep Imaging Multi-Object Spectrograph on the 10m Keck II Telescope (DEIMOS; PI Gordon, Program O438; Faber et al. 2003). The observations totaled 6x300s in *R* band. However, due to high humidity and the crowded nature of the field, guiding proved difficult and thus only three of the images were reliable enough for reduction and analysis. The data were reduced using a custom pipeline based on FSWARP (Bertin et al. 2002). The final image had a limiting magnitude of 24.6. We detected two host candidates close to the localization region at R.A., Decl. = 00:48:23.9121, 42:00:21.954 and 00:48:24.2010, 42:00:21.059, respectively. Using a 1'' aperture, we measure a magnitude for the best host candidate of R_{AB} of 22.8 mag (an estimate only, given the crowded field). We present the R-band Keck image of the field of FRB 20230506C in Figure 4.

To confidently determine the host galaxy of FRB 20230506C in the crowded field, we employed ASTROPATH on the Keck R-band image to calculate the probability of its association with the two nearest galaxies. We find the host galaxy of FRB 20230506C, the one coincident with the burst, has a posterior of 0.9722 adopting standard priors for the offset distribution of FRBs (Shannon et al. 2024). The second most likely galaxy has a negligible posterior of 1.095×10^{-4} . The probability that the host is undetected given the depth of the Keck image is similarly negligible. Thus, we conclude the host association to be robust.

We next obtained a spectrum with the Binospec spectrograph at the 6.5m MMT Observatory (PI Nugent, Program UAO-G200-24A; Fabricant et al. 2019) on June 8, 2024 UTC. The slit was placed and aligned to cover the location of both host candidates. We obtained 4x900s of exposure using a one arcsecond slit with the LP3800 filter, 270 lines/mm grating, and a central wavelength of 6500 Angstroms. Similarly to the DEIMOS imaging, the data were plagued by poor observing conditions. When combined with a small astrometric error that shifted the position of the candidates partially out of the slit, we could not detect any emission from either of the host candidates.

We conducted a second spectroscopic observation with the Low Resolution Imaging Spectrometer (LRIS; Oke et al. 1995) on the 10m Keck I telescope on September 6, 2024 UTC (PI Ravi, Program C382). Observing conditions were excellent and seeing was near 0.5''. We

obtained 2x1800s and 4x900s exposures with the blue and red detectors, respectively. The blue spectrum is produced with a grism with 400 lines/mm at 3400Å and the red side by a grating with 400 lines/mm at 8500Å. The slit was oriented to cover the first and second most probable host galaxy. Spectra were calibrated with LPIPE (Perley 2019). The 1d spectral extraction was done with a boxcar and integrated over the slit.

Figure 4 shows the spectrum and model fits. Both continuum and strong line emission are evident throughout the spectrum. As before, the best-fit model and redshift were found with the spectral modeling code PPXF. Based on fits with strong emission lines from the Balmer series, [OII], and [OIII], we find a host redshift of 0.3896 ± 0.0002 . The spectrum for the second closest candidate host shows no significant spectral features.

Table 2 shows the line fluxes for the best-fit model. Only lines with a significance greater than 5 are shown. Using the ratio of $H\alpha$ to $H\beta$, we estimate an extinction $E(B-V) = 0.064$. The ppxf modeled line fluxes are corrected for extinction using DUST_EXTINCTION (Gordon 2024).

We estimated the stellar mass using PROSPECTOR (Johnson et al. 2021) spectral energy distribution modeling, jointly fitting the observed photometry and spectroscopy and assuming a delayed τ parametric star formation history. We find the stellar mass to be $\log M_* = 8.91_{-0.19}^{+0.20} M_{\odot}$. The SFR and sSFR for this galaxy are also listed in Table 2.

3. DM BUDGET

The DM contribution from M31 can be estimated using the DM budget of the FRBs. The total DM measured for the FRBs can be written as:

$$DM_{\text{obs}} = DM_{\text{MW,disk}} + DM_{\text{MW,halo}} + DM_{\text{M31}} + DM_{\text{IGM}} + \frac{DM_{\text{host}}}{1+z} \quad (1)$$

Therefore, by modeling the DM contribution from disk and halo of Milky Way ($DM_{\text{MW,disk}}$ and $DM_{\text{MW,halo}}$), intergalactic medium (DM_{IGM}) and the host galaxy (DM_{host}), we can estimate the DM contribution from M31 (DM_{M31}). The probability density function (PDF) of the sum of independent variables can be written as the convolution of the PDF of each variable. Therefore from equation 1, we can write:

$$\begin{aligned} \mathcal{P}(DM_{\text{M31}}) = & \mathcal{P}(DM_{\text{obs}}) * \mathcal{P}(-DM_{\text{MW,disk}}) \\ & * \mathcal{P}(-DM_{\text{MW,halo}}) * \mathcal{P}(-DM_{\text{IGM}}) \\ & * \mathcal{P}(-DM_{\text{host}}) \end{aligned} \quad (2)$$

Since the FRBs have asymmetric uncertainties on their observed DM values, we model $\mathcal{P}(DM_{\text{obs}})$ as a

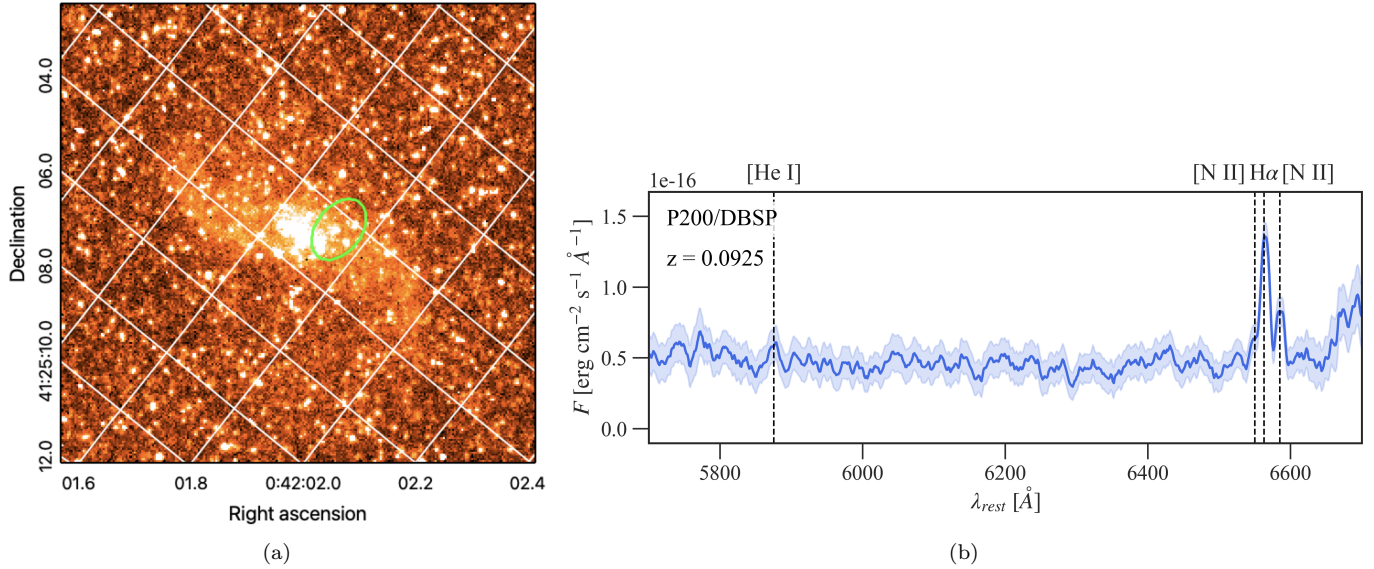


Figure 3. (a) The HST/WCS image of the host galaxy of FRB 20230930A. The 5σ *realfast* localization region is shown in green. (b) The DBSP spectrum of the host galaxy of FRB 20230930A.

Properties	HG FRB 20230930A	HG FRB 20230506C
Alt. Name	PSO J010.5070+41.4175	-
RA	00h42m01.676s	00h48m23.9121s
Dec	41°25′3.143″	42°00′21.954″
z	0.0925 ± 0.0002	0.3896 ± 0.0002
$M_*(M_\odot)$	$9.1^{+1.0}_{-1.6} \times 10^9$	$(8.1 \pm 1.5) \times 10^8$
$L_{H\alpha}$ (ergs s^{-1})	3.4×10^{40}	7.0×10^{40}
SFR ($M_\odot yr^{-1}$)	0.19	0.38
sSFR (yr^{-1})	$(2.05 \pm 0.36) \times 10^{-11}$	$(4.7 \pm 0.9) \times 10^{-10}$
H α (erg $cm^{-2}s^{-1}$)	1.48×10^{-15}	$1.24(6) \times 10^{-16}$
H β (ergs $cm^{-2}s^{-1}$)	-	$4.4(3) \times 10^{-17}$
[OII] 3726 (ergs $cm^{-2}s^{-1}$)	-	$4.5(5) \times 10^{-17}$
[OII] 3729 (ergs $cm^{-2}s^{-1}$)	-	$6.7(5) \times 10^{-17}$
[OIII] 5007 (ergs $cm^{-2}s^{-1}$)	-	$1.6(6) \times 10^{-16}$
$M_{HI}(M_\odot)(z = 0.08)$	$< 1 \times 10^{10}$	-
N_{HI} (cm^{-2})	1.05×10^{21}	1.7×10^{21}

Table 2. Observed and derived properties of the host galaxies of the FRBs. Emission-line fluxes for the host of FRB 20230506C have been corrected for the measured Balmer decrement and Galactic extinction; for the host of FRB 20230930A, only Galactic extinction was applied.

split-normal PDF where μ is the central value of the DM and σ_1 is the standard deviation below μ and σ_2 is the standard deviation above μ . Here, for FRB 20230930A, we take $\mu = 456$ pc cm^{-3} , $\sigma_1 = 0.6$ and $\sigma_2 = 0.5$ pc cm^{-3} and for FRB 20230506C, $\mu = 772$ pc cm^{-3} , $\sigma_1 = 2$ and $\sigma_2 = 3$ pc cm^{-3} .

3.1. DM from Milky Way

The Milky Way disk contribution to the DM in the line of sight of the FRBs can be obtained from elec-

tron density distribution models like NE2001 (Cordes & Lazio 2002). For FRB 20230930A the $DM_{MW,disk} = 70$ pc cm^{-3} and for FRB 20230506C it is 68 pc cm^{-3} from the NE2001 (Cordes & Lazio 2002) model. To constrain the uncertainty on the NE2001 model estimation, we examined the DMs of nearby pulsars. The closest pulsar to both FRBs ($\sim 6^\circ$ away) J0039+35 has a DM of 53 pc cm^{-3} and this sets a lower limit to the line of sight Milky-Way disk contribution. The distance to this pulsar remains unconstrained, rendering

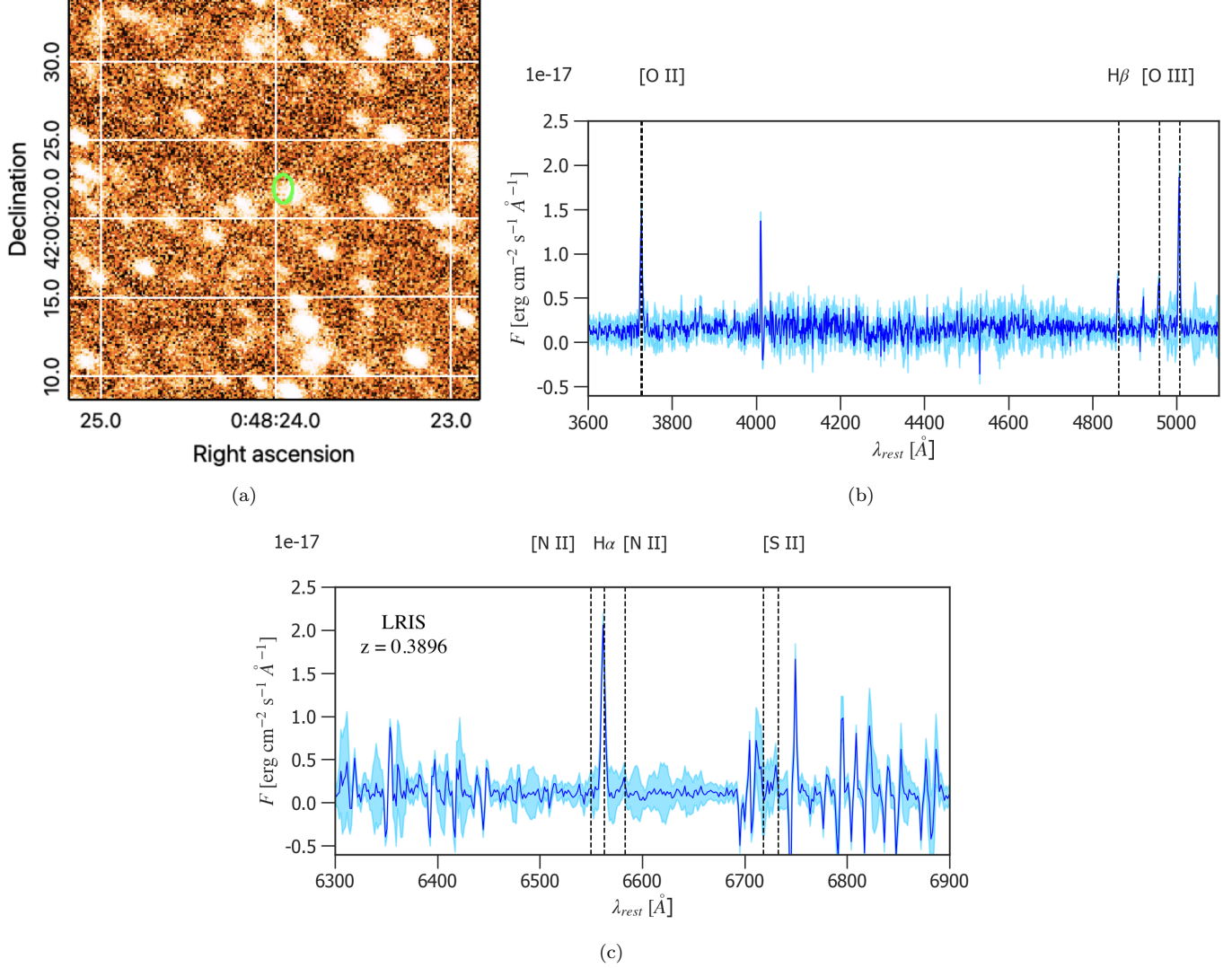


Figure 4. (a) The Keck R -band image of the host galaxy of FRB 20230506C. The 5σ *realfast* localization region is shown in green. (b) The blue region and (c) the red region, of Keck LRIS spectrum of the host galaxy of FRB 20230506C. The redder spectrum had a poor subtraction of telluric features, but we limit our analysis to the features labeled with dashed lines.

it ineffective for reducing the uncertainty in the NE2001 model estimation. To estimate the uncertainty on the Milky Way DM from the NE2001 and YMW16 (Yao et al. 2017) models, we then identified pulsars from the PSR π sample (Deller et al. 2019), with independent distance measurements, that were within $\sim 20^\circ$ of the position of the FRBs. We found three pulsars J0040+5716, J0055+5117, and J0147+5922 within this region. Although NE2001 slightly underestimates the DM for J0147+5922, it over predicts the DM of the other two pulsars by a factor of two, until their measured distances (see Table 3). It is worth noting that J0147+5922 has the lowest Galactic latitude ($b = -2.7$) of all the three pulsars and the FRBs.

To account for these systematic discrepancies, we assume a 30% uncertainty on the Milky Way disk DM

Pulsar	DM _{measured} (pc cm^{-3})	Distance (kpc)	DM _{predicted} (pc cm^{-3})
J0040+5716	92.6	9.77	183.3
J0055+5117	44.1	2.87	71.1
J0147+5922	40.1	2.02	31.8

Table 3. PSR π pulsars within 20° of the line of sight of both FRBs. The predicted DM is from NE2001 model.

contribution. Therefore, $\mathcal{P}(\text{DM}_{\text{MW,disk}})$ is a truncated Gaussian distribution with a lower limit set at 53 pc cm^{-3} , $\mu = 70 \text{ pc cm}^{-3}$ and $\sigma = 21 \text{ pc cm}^{-3}$ for FRB 20230930A and $\mu = 68 \text{ pc cm}^{-3}$ and $\sigma = 20$ for the FRB 20230506C. For the Milky Way halo, we assume a Gaussian distribution with $\mu = 38 \text{ pc cm}^{-3}$ and

$\sigma = 19 \text{ pc cm}^{-3}$ corresponding to a 50% uncertainty (Ravi et al. 2023).

3.2. DM from the IGM

We calculate the average $\text{DM}_{\text{cosmic}}$ using equation (2) in Macquart et al. (2020). We use the same prescription to calculate the probability density and use the values $\alpha = 3.0$ and $\beta = 3.0$ for the parameters describing the inner halo density profile and feedback parameter $F = 0.31$.

3.3. DM from host galaxies

Although host galaxies are expected to contribute significantly to the total DM of FRBs, estimating this contribution is challenging. $\text{H}\alpha$ surface density can trace the emission measure and, in principle, the DM. However, this estimate depends on several factors—such as the gas temperature, the clumpiness of the $\text{H}\alpha$ -emitting regions, and the FRB’s path length through the host—resulting in a potentially wide range of $\text{DM}_{\text{host,disk}}$ that can overlap with the observed total DM.

Using a large sample of cosmological FRBs, Connor et al. (2024) found that DM_{host} is well described by a log-normal distribution with $\mu = 4.90^{+0.18}_{-0.20}$ and $\sigma = 0.53^{+0.16}_{-0.14}$. We therefore adopt the same log-normal prior for our host galaxies. This also includes the contribution from the host’s halo.

3.4. DM from M31

To convolve different PDFs, it is essential to assume that each PDF is independent of the others. To verify this assumption, we performed Monte Carlo sampling for each DM component from its respective distribution and computed the pairwise Pearson correlation coefficients. The largest correlation coefficient was found to be 0.003, indicating that the DM components can be considered independent.

We defined the PDF of each component as described above, imposing a zero probability for negative DM values, followed by normalization. The PDF of DM_{M31} was then computed via the convolution in Equation 2. probability of any negatives in DM_{M31} were again set to zero and the distribution renormalized, from which the median and CIs were derived. We adopt a 90% CI, rather than the more commonly used 68%, to provide a more conservative characterization of our asymmetric posterior distribution. The resultant distribution is shown in Figure 5 and the values are listed in Table 5.

3.5. Independent DM constraints on M31

The M31 DM we determined in the above section is the sum total of the DM contribution from its disk and

Constant	value	units
A_d	2500	pc
B_d	15000	pc
K_2	1.54	
A_2	1200	pc
B_2	4000	pc
H_1	1673	pc
$n_{\text{thick},0}$	0.01131	cm^{-3}
$n_{\text{thin},0}$	0.404	cm^{-3}

Table 4. The assumed values for the disk modeling of M31. The values are taken from (Yao et al. 2017)

halo. In this section, we identify the individual contribution to the total DM from the disk and halo. To make sure that the FRB line of sight is not intersecting any regions of excess electron density, we compared the positions of the FRBs with respect to the HII regions of M31. Ocker et al. (2024) has revealed that HII regions can contribute tens to hundreds of DM units depending up on the path length intersecting the region. It is clear from the Figure 6, that the FRB sight-lines do not intersect any cataloged HII regions or planetary nebulae in M31 (Azimlu et al. 2011) and therefore the DM_{M31} might not be dominated by any over dense regions.

3.5.1. M31 Disk DM

We modeled the electron density distribution of the thin and thick disk of M31 as a function of radial and vertical distance, assuming it is similar to the Milky Way using the models from Yao et al. (2017). The thick disk was modeled using the equation

$$n_{\text{thick}} = n_{\text{thick},0} g_d \text{sech}^2 \left(\frac{z}{H_1} \right) \quad (3)$$

where $n_{\text{thick},0}$ and H_1 is the mid plane density and scale height respectively. The vertical and the radial extent of the disk is set by the parameters A_d and B_d . For $R \leq B_d$, $g_d = 1$ and for $R > B_d$, $g_d = \text{sech}^2 \left(\frac{R-B_d}{A_d} \right)$. The electron density of the thin disk is modeled by the equation

$$n_{\text{thin}} = n_{\text{thin},0} g_d \text{sech}^2 \left(\frac{R-B_2}{A_2} \right) \text{sech}^2 \left(\frac{z}{K_2 H} \right) \quad (4)$$

where H is the parameterized scale height on R given by:

$$H = 32 + 1.3 \times 10^{-3} R + 4.0 \times 10^{-7} R \quad (5)$$

The Table 4 lists the values of the constants used.

The total electron density of the M31 disk is, $n_{\text{total}} = n_{\text{thick}} + n_{\text{thin}}$. We take the center of M31 as the origin and the LOS of the FRBs are inclined to the plane

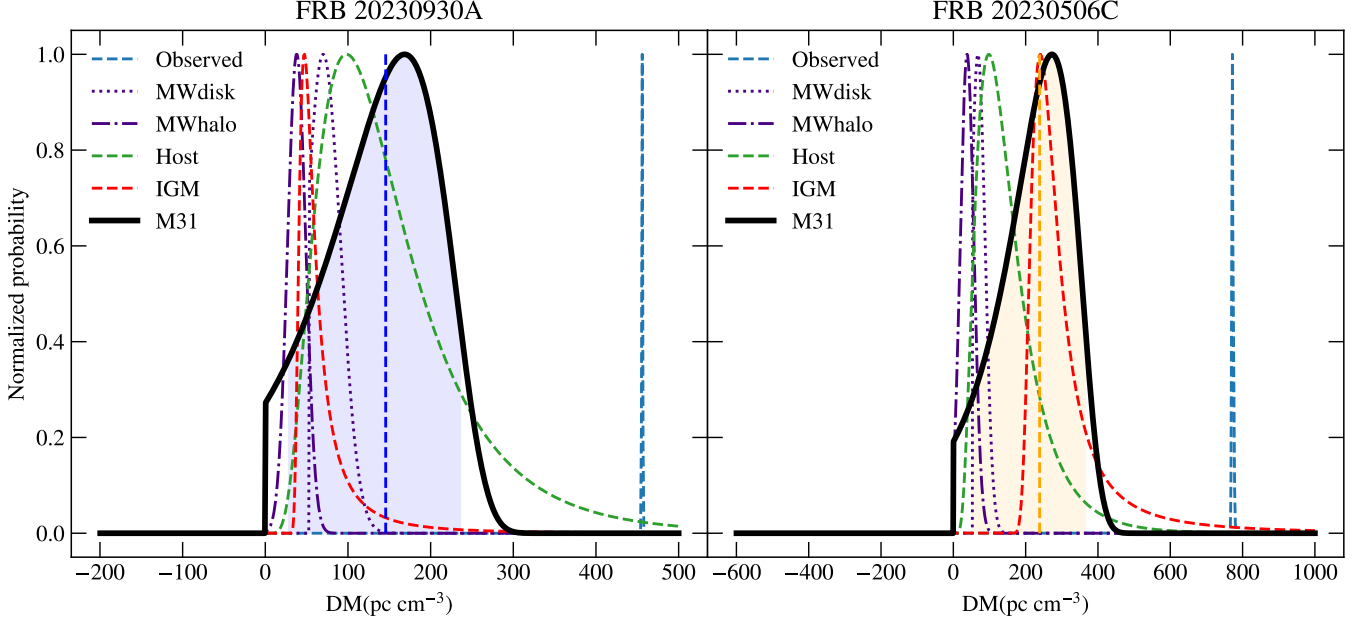


Figure 5. The probability distribution of all different DM components. The *left* panel corresponds to FRB 20230930A and the *right* panel to FRB 20230506C. The blue line shows the PDF of the observed DM. The indigo dotted line represents the MW disk contribution, while the dash-dot line represents the MW halo. The green dashed line corresponds to the host DM distribution, the red line to the IGM distribution, and the black line to M31. In the left panel, the dark blue dashed vertical line marks the median of the DM_{M31} distribution, with the shaded region indicating the 90% CI. In the right panel, the orange dashed vertical line marks the median, and the shaded region likewise denotes the 90% CI

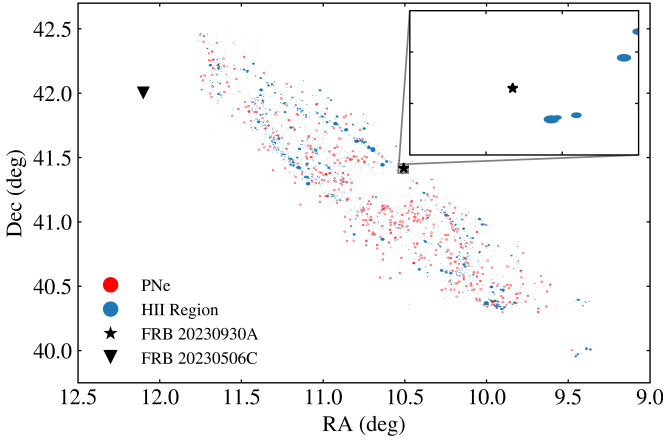


Figure 6. The map of HII regions and Planetary nebula of M31 with respect to the FRB lines of sight. The region zoomed around FRB 20230930A is shown in the inset. The size of the HII regions and planetary nebulae circles are scaled by their actual size. The catalog is adapted from [Azimlu et al. \(2011\)](#).

of M31 at an angle of 12.5° ([Simien et al. 1978](#)). For FRB 20230930A, a projected impact parameter of 2.7 kpc corresponds to a galactocentric radius of 12.5 kpc within M31's disk. By integrating the total electron density n_{total} along the line of sight that crosses the disk

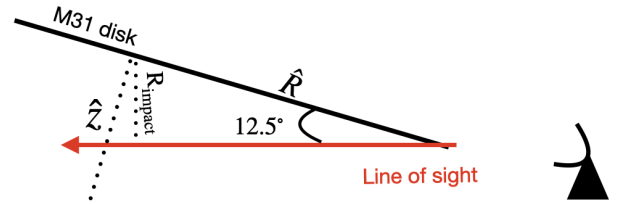


Figure 7. The geometry of M31's disk with respect to the FRB 20230930A's line-of-sight. The DM from M31's disk is calculated by integrating the electron density $n_e(R, z)$ along this line-of-sight.

vertically at this radius in the z - R (Fig. 7), we estimate a disk contribution $DM_{M31, \text{disk}} = 128 \text{ pc cm}^{-3}$. At an impact parameter of 17.1 kpc, the M31 disk contributes negligibly to the DM of FRB 20230506C. In this modeling, we assumed that M31 is analogous to the Milky Way, and disregarded the contributions from spiral arms and other galactic components. To account for this in addition to the inherent uncertainties in the YMW16 model, we assume a 50% uncertainty on the calculation.

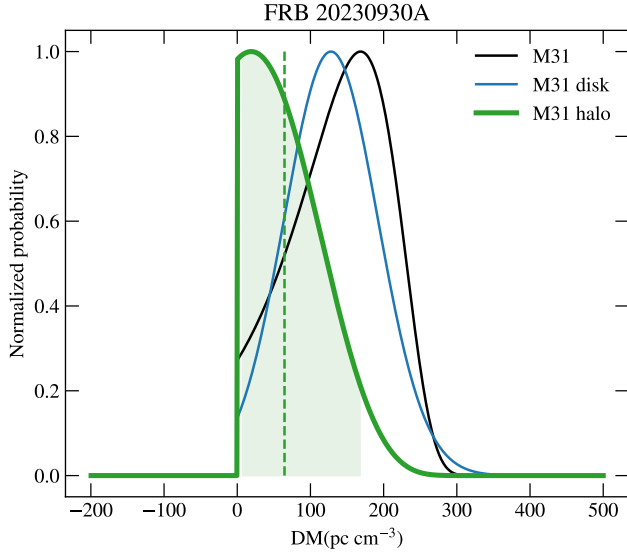


Figure 8. The $DM_{M31,halo}$ estimated from FRB 20230930A. The total DM_{M31} is shown in black, with the $DM_{M31,disk}$ in blue and the $DM_{M31,halo}$ in green. The dashed green line marks the median of the $DM_{M31,halo}$ PDF for FRB 20230930A, and the shaded region indicates the 90% CI.

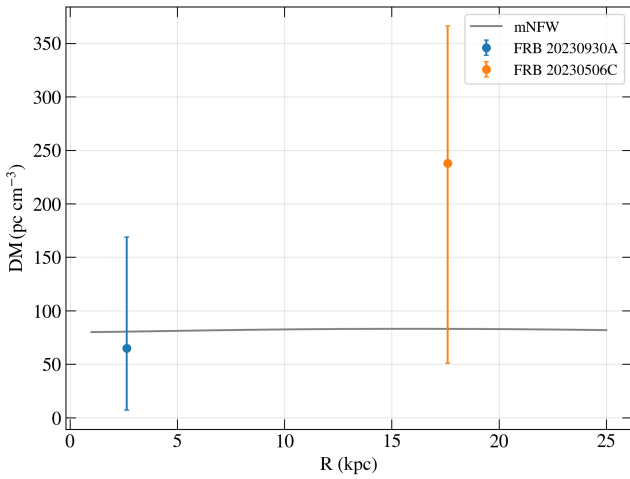


Figure 9. The DM predicted from mNFW profile of M31's halo for a given impact parameter from the center of the halo (grey). The $DM_{M31,halo}$ measured from the two FRBs are also shown. The FRB measurements are centered on the median and extends to the 90% CIs.

3.6. M31 halo DM

The estimation of $DM_{M31,disk}$ allows us to isolate the $DM_{M31,halo}$ from the total DM_{M31} . The PDF of $DM_{M31,halo}$ (see Figure 8) can be written as:

$$\mathcal{P}(DM_{M31,halo}) = \mathcal{P}(DM_{M31}) * \mathcal{P}(-DM_{M31,disk}) \quad (6)$$

M31's contribution to the DM of the FRBs from its CGM is given in Table 5.

We then compared this estimate with the theoretical predictions of M31's halo profile from the mNFW profile (Mathews & Prochaska 2017). From the mNFW profile, we can estimate the halo DM for the FRBs given their impact parameter (Prochaska & Zheng 2019). The mNFW density profile is given by:

$$\rho_b = \frac{\rho_b^0}{y^{1-\alpha}(y_0 + y)^{2+\alpha}} \quad (7)$$

where $y \equiv c(r/r_{200})$, where c is the concentration parameter and r_{200} is the virial radius, $\rho_b^0 = (200\rho_c/3)c^3/f(c)$, $f(y) = \ln(1+y) - y/(1+y)$, $\rho_c = 9.2 \times 10^{-30} \text{ g cm}^{-3}$ is the critical density for the Hubble constant $H_0 = 70 \text{ km s}^{-1}$, y_0 is a feedback-dependent parameter, and α is a constant (Mathews & Prochaska 2017). Following Prochaska & Zheng (2019), we set $\alpha = 2$ and $y_0 = 2$, and a constant $c = 7.67$ for M31. The DMs of FRBs traveling through a halo are dependent upon the impact parameter as is given by

$$DM(R_\perp) = 2 \int_0^{\sqrt{r_{max}^2 - R_\perp^2}} n_e ds \quad (8)$$

Figure 8 shows the measured DM contribution from the halo of M31 using FRB 20230930A and Figure 9 shows the DM profile as predicted by mNFW. The mNFW halo DM contribution is consistent with the observed DM_{halo} within the CIs for FRB 20230930A and FRB 20230506C.

4. DISCUSSION

We have estimated the DM contribution of M31 along the line of sights probed by FRB 20230930A and FRB 20230506C. After modeling the disk component of M31 along the line of sight of FRB 20230930A, we find that the halo of M31 alone contributes between 7 – 169 pc cm^{-3} . For the FRB 20230506C, we do not expect any contribution from the M31 disk and hence the DM excess corresponds to 51 – 366 pc cm^{-3} . While the lower end of range is consistent with expectation from mNFW and overlaps with the distribution of $DM_{M31,halo}$ from FRB 20230930A, the overall intervals show noticeable differences. We note that FRB 20230506C is a repeating FRB hosted by a low-mass, star-forming galaxy, which may contribute a substantial DM_{host} (Leung et al. 2025). Additional possibilities for foreground contributions are discussed in §4.1.

The halo of M31 has been observed in temperatures up to $T \sim 10^{5.5} \text{ K}$ associated with warm ions like OVI. However, the hotter $T > 10^6 \text{ K}$ ions are expected to

FRB	DM _{M31}		DM _{M31,halo}	
	Value (pc cm ⁻³)	90% CI (pc cm ⁻³)	Value (pc cm ⁻³)	90% CI (pc cm ⁻³)
FRB 20230930A	144	[26, 239]	65	[7, 169]
FRB 20230506C	238	[51, 366]	–	–

Table 5. Comparison of DM_{M31} (left) and DM_{M31,halo} (right) as measured from two *realfast* FRBs. For FRB 20230930A, the M31 disk contribution has been modeled and removed when computing DM_{M31,halo}.

be the dominant contributor to the DM of the halos (Prochaska & Zheng 2019), which are yet to be observationally detected in M31. We looked at the possible contribution to the DM_{M31,halo} from cool ions. The cool phase gas in the halo can be probed using HI high velocity clouds (HVC) or cool ions like SiII, SiIII. These can trace the gas at $T \sim 10^4$ K. The HVCs of M31 were obtained from Westmeier et al. (2008). Given the hydrogen column density of HVCs, the electron column density can be estimated as:

$$N_{e,\text{cool}} = \mu_e N_{\text{HI,HVC}} \left(\frac{1 - \chi_{\text{HI}}}{\chi_{\text{HI}}} \right) \text{ cm}^{-2} \quad (9)$$

where $\mu_e = 1.167$ is the reduced mass for fully ionized hydrogen and helium and the hydrogen neutral fraction $\chi_{\text{HI}} = M_{\text{HI}} / (M_{\text{HI}} + M_{\text{HII}}) = 0.3$, which is commonly used in Milky Way halo estimates (Prochaska & Zheng 2019). The closest HVC is separated by 0.4° to FRB 20230930A and 0.5° to FRB 20230506C, yielding DM_{cool} = 4 pc cm⁻³ and 2 pc cm⁻³ respectively. If, instead, we assume a lower neutral fraction, $\chi_{\text{HI}} = 0.1$ (Thilker et al. 2004), the corresponding contributions increase to DM_{cool} = 17 pc cm⁻³ and 10 pc cm⁻³ for FRB 20230930A and FRB 20230506C respectively. These values overlap with the lower end of the 90% CI of the DM_{M31,halo} measurement from FRB 20230930A. We emphasize, however, that $\chi_{\text{HI}} = 0.1$ is only an estimate and not a direct measurement (Thilker et al. 2004) and thus associated DM values should be treated as an upper limit. Consequently Lehner et al. (2015) reports that the ionization increases with the radius, making the outer halo much more ionized than the inner halo. Therefore, adopting $\chi_{\text{HI}} = 0.3$ is likely more appropriate for our DM_{halo} estimates in the inner halo.

Prochaska & Zheng (2019) also finds a direct correlation between the DM values from N_{HI} and Si ions. Therefore, we also estimate the DM_{cool} from the average contribution of Si ions. We have $\langle N_{\text{Si}} \rangle = 2.5 \times 10^{13} \text{ cm}^{-2}$ at $R < 25$ kpc (Lehner et al. 2015). Here $\langle N_{\text{Si}} \rangle$ is the average of N_{SiII} + N_{SiIII}. Si also has a covering fraction of about unity within $R < 0.2R_{\text{vir}}$ (Lehner et al. 2020).

To estimate the DM, we can write

$$N_e \approx 1.2N_{\text{H}} \quad (10)$$

$$N_{\text{H}} = \frac{N(\text{Si})}{Z \times (\text{Si}/\text{H})_{\odot}} \quad (11)$$

The metallicity in the CGM of M31 is undetermined, however a lower limit of $Z > 0.2Z_{\odot}$ is estimated (Lehner et al. 2020) and we assume $(\text{Si}/\text{H})_{\odot} = 10^{-4.49}$ (Asplund et al. 2009). We get $N_{\text{H}} = 3.8 \times 10^{18} \text{ cm}^{-2}$ and converting this to DM, we get DM_{cool,Si} < 2 pc cm⁻³, thereby confirming our conclusion that cool halo gas does not contribute significantly to the total DM.

We also estimated the DM contribution from the warm component of M31's CGM traced by OVI and CIV. Lehner et al. (2013) studied the cool CGM of nearby galaxies and found that metallicities exhibit a bimodal distribution ranging from $Z/Z_{\odot} = 0.01 - 3$, with the higher end associated with massive outflows. However, studies of M31's CGM by Lehner et al. (2020) indicate that, due to the lack of nucleosynthetic effects on the abundances of elements such as Fe and C relative to Si, the metallicity of M31's CGM is likely sub-solar but not significantly below $1/3 Z_{\odot}$. Additionally, ionization fractions can also vary from sightline-to-sightline; for example, OVI can originate in non-equilibrium cooling layers, turbulent mixing layers, or photoionized streams, resulting in ion fractions that can vary by factors of a few (Oppenheimer & Schaye 2013). Therefore, we assumed a range of values for $Z/Z_{\odot} = 0.1 - 0.5$ and ionization fraction $\chi_{\text{ion}} = 0.1 - 0.9$. For CIV, we used the average column density within $R < 25$ kpc from Lehner et al. (2015) and the solar carbon abundance $(\text{C}/\text{H})_{\odot} = 10^{-3.57}$ (Asplund et al. 2009) and a covering fraction of 0.8 (Lehner et al. 2015), obtaining a 90% CI upper bound of DM_{warm,CIV} < 6 pc cm⁻³. Similarly for OVI, the solar oxygen abundance $(\text{O}/\text{H})_{\odot} = 10^{-3.31}$ (Asplund et al. 2009) and a covering fraction of 1 (Lehner et al. 2015), we find the upper bound to be DM_{warm,OVI} < 5 pc cm⁻³. We note here that for OVI we assumed a covering fraction of 1 based on only two quasar sightlines from Lehner et al. (2015) and therefore the value for OVI should be considered as an upper limit.

Taken together, the cool and warm CGM components contribute at most $\sim 15 \text{ pc cm}^{-3}$ along FRB 20230930A and $\sim 13 \text{ pc cm}^{-3}$ along FRB 20230506C, for $\chi_{\text{HI}} = 0.3^3$. For FRB 20230930A, this contribution only grazes the lower edge of the 90% CI, while for FRB 20230506C it falls far short of the observed excess. Thus, the cool and warm phase gas is unlikely to account for the measured $\text{DM}_{\text{M31,halo}}$. An additional component, most plausibly a hot, ionized halo, is likely required. Our results therefore provide indirect evidence for the presence of a hot gaseous halo around M31, along at least two sight-lines.

4.1. Other foreground contributions

The other possibility for the estimated $\text{DM}_{\text{M31,halo}}$ is the hot bridge connecting M31 and MW. There are detections of a large scale ($r \sim 20^\circ$) X-ray and SZ bright hot plasma bridge between the MW and M31, with length 400 kpc and radius of 120 kpc (Qu et al. 2021). Even though, it is not a part of the M31 halo, the bridge could potentially contribute to the DM of the FRB. This plasma bridge has an electron number density of $2 \times 10^{-4} - 10^{-3} \text{ cm}^{-3}$, for a length of 400 kpc, this can contribute $\text{DM} = 80 - 400 \text{ pc cm}^{-3}$. We note, however, that the reported X-ray and SZ detections are at $< 5\sigma$ significance (Qu et al. 2021), and the geometry of the intersection strongly affects the actual DM contribution. Although the distribution of the $\text{DM}_{\text{M31,halo}}$ measurement from the FRBs are broadly consistent with the theoretical predictions of mNFW, FRB 20230506C exhibits only weak consistency. Therefore, it is plausible that the line of sight of FRB 20230506C has intersected the plasma bridge.

The Triangulum galaxy, M33, is the third massive spiral galaxy in the local group, along with Milky Way and M31. We investigated whether M33 would contribute to the DM of these FRBs. We find that the FRBs in our sample are located approximately 14.5 degrees away from the position of M33, corresponding to a projected distance of 213 kpc. Given that the virial radius of M33's halo is roughly 168 kpc (Zacharie Kam et al. 2017), the FRB sightline lies well from outside the central halo region, and we therefore expect negligible contribution from M33 alone to the foreground DM, although we cannot rule out a contribution from shared plasma of M33 and M31 along the line of sight.

The Milky Way, M31, M33, and their numerous satellite galaxies, including the Magellanic Clouds, are all part of the Local Group. Theoretically, these galaxies

are expected to be embedded in an ionized intragroup medium; however, no cool or hot intragroup medium has yet been detected observationally. We expect a potential degeneracy between the DM attributed to M31 and that from the intra-group medium. Nevertheless, Huang et al. (2025), using the HESTIA simulations, modeled the DM from the Milky Way halo and the Local Group medium, and found only a negligible contribution (2 pc cm^{-3}) from the intra-group medium beyond that associated with the spiral galaxies and their satellites.

We note that we have not systematically searched for other foreground halos, which could contribute additional DM components. This is especially important for the FRB 20230506C, given its larger distance.

5. CONCLUSION

In this paper, we report on the *realfast* discovery of two FRBs that pierce both the halo and the disk of M31. We detected repeat bursts from FRB 20230506C. Optical follow-up identified the host of FRB 20230930A at a redshift, $z = 0.0925$ and the host of FRB 20230506C at a redshift of $z = 0.3896$. We used the DM budget of these FRBs to constrain the electron density distribution of M31's halo.

- The Milky Way disk contribution was estimated from NE2001 model and a lower limit on the error bar was chosen based on the DM of the nearest pulsar.
- After modeling out the DM contributions from the Milky Way, the IGM and the host galaxies, we isolated the total DM_{M31} in the lines-of-sight of both FRBs. The 90% CIs for the total DM_{M31} can range from $26 - 239 \text{ pc cm}^{-3}$ and $51 - 366 \text{ pc cm}^{-3}$ for FRB 20230930A and FRB 20230506C, respectively.
- We then modeled the disk of M31 using a Milky Way analog of YMW16 electron density model. After subtracting the disk contribution from the total DM_{M31} , we obtained the PDF of the DM contribution from the CGM of M31, $\text{DM}_{\text{M31,halo}}$. While the M31's disk contribution to the total DM of FRB 20230506C was found to be zero, the non zero contribution to the FRB 20230930A constrained the $\text{DM}_{\text{M31,halo}}$ along that line of sight to be between 7 and 169 pc cm^{-3} .
- We compared our measurements to the predictions from the mNFW profile of M31's halo and find that it is broadly consistent within the CIs for both FRBs.

³ For $\chi_{\text{HI}} = 0.1$, this becomes at most 28 and 21 pc cm^{-3} for FRB 20230930A and FRB 20230506C, respectively

- The measured $DM_{M31,halo}$, along these two sightlines, is consistent with the presence of a hot gaseous halo around M31, as contributions from the cool and warm phases alone are unlikely to explain the observed values.
- The other possibility that can account for the excess in $DM_{M31,halo}$ along FRB 20230506C is if its line of sight intersects the plasma bridge between MW and M31. We also discuss the possibility of additional DM contribution from M33 and the local group medium and finds it to be negligible.

In this work, we have demonstrated how FRBs can be used to study the CGM of nearby galaxies. Higher time resolution and polarimetric follow-up of the repeating FRB 20230506C will help constrain the turbulence and magnetization of the halo by measuring properties such as scattering and rotation measure (Prochaska et al. 2019).

Instruments such as CHIME are expected to detect and localize hundreds of FRBs intersecting M31, enabling a detailed reconstruction of its DM profile, particularly in the outer halo where our current constraints are limited. Improved estimates of DM_{host} , are also crucial for establishing more informative priors. Integral Field Spectroscopy of FRB host galaxies (Bernales-Cortes et al. 2025) offers a promising path forward, as spatially resolved maps of ionized gas can reveal whether an FRB resides within a dense, ionized clump that contributes significantly to DM_{host} or instead lies in a comparatively diffuse environment.

6. ACKNOWLEDGMENTS

We thank the anonymous referee for valuable suggestions. We also thank Nicolas Lehner and Zhijie Qu for useful discussions. RAT and SBS were supported in this work by NSF award #1714897. RAT acknowledges funding for this work from the European Research Council (ERC) under the European Union's Horizon 2020 research and innovation programme ('EuroFlash'; Grant agreement No. 101098079). SBS gratefully acknowledges the support of a Sloan Fellowship. CJL acknowledges support from the National Science Foundation under Grant No. 2022546. *realfast* is supported by the NSF Advanced Technology and Instrumentation program under award 1611606. Computational resources were provided by the WVU Research Computing Dolly Sods HPC cluster, which is funded in part by NSF MRI Grant #2117575. A.C.G. and the Fong Group at Northwestern acknowledges support by the National Science Foundation under grant Nos. AST-1909358, AST-

2308182 and CAREER grant No. AST-2047919. A.C.G. acknowledges support from NSF grants AST-1911140, AST-1910471 and AST-2206490 as a member of the Fast and Fortunate for FRB Follow-up team. LC is grateful for support from NSF grants AST-2205628 and AST-2107070.

The Green Bank and National Radio Astronomy Observatories are facilities of the National Science Foundation operated under cooperative agreements by Associated Universities, Inc. We thank the telescope operators and project friends during all our VLA and GBT observations.

The Local Group L-Band survey (LGLBS) is an Extra Large program conducted on Jansky Very Large Array, which is operated by the National Radio Astronomy Observatory (NRAO) and includes observations from VLA projects 20A-346, 13A-213, 14A-235, 14B-088, 14B-212, 15A-175, 17B-162, and GBT projects 09A-017, 13A-420, 13A-430, 13B-169, 14A-367, 16A-413. Execution of the LGLBS survey science was supported by NSF Award 2205628.

W. M. Keck Observatory and MMT Observatory access was supported by Northwestern University and the Center for Interdisciplinary Exploration and Research in Astrophysics (CIERA).

Some of the data presented herein were obtained at the W. M. Keck Observatory, which is operated as a scientific partnership among the California Institute of Technology, the University of California and the National Aeronautics and Space Administration. The Observatory was made possible by the generous financial support of the W. M. Keck Foundation.

The authors wish to recognize and acknowledge the very significant cultural role and reverence that the summit of Maunakea has always had within the indigenous Hawaiian community. We are most fortunate to have the opportunity to conduct observations from this mountain.

Observations reported here were obtained at the MMT Observatory, a joint facility of the Smithsonian Institution and the University of Arizona.

7. DATA AVAILABILITY

The scripts and notebooks used to reproduce the results and figures are available at the GitHub repository https://github.com/ReshmaAnnaThomas/realfast_M31_FRBs_paper. The necessary data products will be linked in the same directory or can be obtained upon request from the author. This work made use of RFPipe <https://github.com/realfastvla/rfpipe>, example *realfast* localization scripts are available at https://github.com/ReshmaAnnaThomas/realfast_localization.

REFERENCES

- Agarwal, D., Aggarwal, K., Burke-Spolaor, S., Lorimer, D. R., & Garver-Daniels, N. 2020, *MNRAS*, 497, 1661, doi: [10.1093/mnras/staa1856](https://doi.org/10.1093/mnras/staa1856)
- Aggarwal, K., Agarwal, D., Lewis, E. F., et al. 2021, *ApJ*, 922, 115, doi: [10.3847/1538-4357/ac2577](https://doi.org/10.3847/1538-4357/ac2577)
- Aggarwal, K., Law, C. J., Burke-Spolaor, S., et al. 2020, *Research Notes of the American Astronomical Society*, 4, 94, doi: [10.3847/2515-5172/ab9f33](https://doi.org/10.3847/2515-5172/ab9f33)
- Aggarwal, K., Agarwal, D., Kania, J. W., et al. 2020, *Journal of Open Source Software*, 5, 2750, doi: [10.21105/joss.02750](https://doi.org/10.21105/joss.02750)
- Anna-Thomas, R., Burke-Spolaor, S., Law, C. J., et al. 2024, *ApJ*, 974, 72, doi: [10.3847/1538-4357/ad66c9](https://doi.org/10.3847/1538-4357/ad66c9)
- Asplund, M., Grevesse, N., Sauval, A. J., & Scott, P. 2009, *ARA&A*, 47, 481, doi: [10.1146/annurev.astro.46.060407.145222](https://doi.org/10.1146/annurev.astro.46.060407.145222)
- Azimlu, M., Marciniak, R., & Barmby, P. 2011, *AJ*, 142, 139, doi: [10.1088/0004-6256/142/4/139](https://doi.org/10.1088/0004-6256/142/4/139)
- Barsdell, B. R. 2012, PhD thesis, Swinburne University of Technology
- Bernales-Cortes, L., Tejos, N., Prochaska, J. X., et al. 2025, *A&A*, 696, A81, doi: [10.1051/0004-6361/202452026](https://doi.org/10.1051/0004-6361/202452026)
- Bertin, E., Mellier, Y., Radovich, M., et al. 2002, in *Astronomical Society of the Pacific Conference Series*, Vol. 281, *Astronomical Data Analysis Software and Systems XI*, ed. D. A. Bohlender, D. Durand, & T. H. Handley, 228
- Bhandari, S., Heintz, K. E., Aggarwal, K., et al. 2022, *AJ*, 163, 69, doi: [10.3847/1538-3881/ac3aec](https://doi.org/10.3847/1538-3881/ac3aec)
- Bhardwaj, M., Michilli, D., Kirichenko, A. Y., et al. 2024, *ApJL*, 971, L51, doi: [10.3847/2041-8213/ad64d1](https://doi.org/10.3847/2041-8213/ad64d1)
- Bregman, J. N., Hodges-Kluck, E., Qu, Z., et al. 2022, *ApJ*, 928, 14, doi: [10.3847/1538-4357/ac51de](https://doi.org/10.3847/1538-4357/ac51de)
- Cappellari, M. 2017, *MNRAS*, 466, 798, doi: [10.1093/mnras/stw3020](https://doi.org/10.1093/mnras/stw3020)
- . 2022, arXiv e-prints, arXiv:2208.14974, <https://arxiv.org/abs/2208.14974>
- Chatterjee, S., Law, C. J., Wharton, R. S., et al. 2017, *Nature*, 541, 58, doi: [10.1038/nature20797](https://doi.org/10.1038/nature20797)
- Connor, L., & Ravi, V. 2022, *Nature Astronomy*, 6, 1035, doi: [10.1038/s41550-022-01719-7](https://doi.org/10.1038/s41550-022-01719-7)
- Connor, L., van Leeuwen, J., Oostrum, L. C., et al. 2020, *MNRAS*, 499, 4716, doi: [10.1093/mnras/staa3009](https://doi.org/10.1093/mnras/staa3009)
- Connor, L., Ravi, V., Catha, M., et al. 2023, *ApJL*, 949, L26, doi: [10.3847/2041-8213/acd3ea](https://doi.org/10.3847/2041-8213/acd3ea)
- Connor, L., Ravi, V., Sharma, K., et al. 2024, arXiv e-prints, arXiv:2409.16952, doi: [10.48550/arXiv.2409.16952](https://doi.org/10.48550/arXiv.2409.16952)
- Cook, A. M., Bhardwaj, M., Gaensler, B. M., et al. 2023, *ApJ*, 946, 58, doi: [10.3847/1538-4357/acbbd0](https://doi.org/10.3847/1538-4357/acbbd0)
- Cordes, J. M., & Lazio, T. J. W. 2002, arXiv e-prints, astro, doi: [10.48550/arXiv.astro-ph/0207156](https://doi.org/10.48550/arXiv.astro-ph/0207156)
- Deller, A. T., Goss, W. M., Brisken, W. F., et al. 2019, *ApJ*, 875, 100, doi: [10.3847/1538-4357/ab11c7](https://doi.org/10.3847/1538-4357/ab11c7)
- Faber, S. M., Phillips, A. C., Kibrick, R. I., et al. 2003, in *Society of Photo-Optical Instrumentation Engineers (SPIE) Conference Series*, Vol. 4841, *Instrument Design and Performance for Optical/Infrared Ground-based Telescopes*, ed. M. Iye & A. F. M. Moorwood, 1657–1669, doi: [10.1117/12.460346](https://doi.org/10.1117/12.460346)
- Fabricant, D., Fata, R., Epps, H., et al. 2019, *PASP*, 131, 075004, doi: [10.1088/1538-3873/ab1d78](https://doi.org/10.1088/1538-3873/ab1d78)
- Gordon, A. C., Fong, W.-f., Kilpatrick, C. D., et al. 2023, *ApJ*, 954, 80, doi: [10.3847/1538-4357/ace5aa](https://doi.org/10.3847/1538-4357/ace5aa)
- Gordon, K. D. 2024, *Journal of Open Source Software*, 9, 7023, doi: [10.21105/joss.07023](https://doi.org/10.21105/joss.07023)
- Huang, Y., Lee, K.-G., Libeskind, N. I., et al. 2025, *MNRAS*, 538, 2785, doi: [10.1093/mnras/staf417](https://doi.org/10.1093/mnras/staf417)
- Johnson, B. D., Leja, J., Conroy, C., & Speagle, J. S. 2021, *ApJS*, 254, 22, doi: [10.3847/1538-4365/abef67](https://doi.org/10.3847/1538-4365/abef67)
- Law, C. J., Bower, G. C., Burke-Spolaor, S., et al. 2015, *ApJ*, 807, 16, doi: [10.1088/0004-637X/807/1/16](https://doi.org/10.1088/0004-637X/807/1/16)
- . 2018, *ApJS*, 236, 8, doi: [10.3847/1538-4365/aab77b](https://doi.org/10.3847/1538-4365/aab77b)
- Law, C. J., Butler, B. J., Prochaska, J. X., et al. 2020, *ApJ*, 899, 161, doi: [10.3847/1538-4357/aba4ac](https://doi.org/10.3847/1538-4357/aba4ac)
- Law, C. J., Sharma, K., Ravi, V., et al. 2024, *ApJ*, 967, 29, doi: [10.3847/1538-4357/ad3736](https://doi.org/10.3847/1538-4357/ad3736)
- Lehner, N., Howk, J. C., & Wakker, B. P. 2015, *ApJ*, 804, 79, doi: [10.1088/0004-637X/804/2/79](https://doi.org/10.1088/0004-637X/804/2/79)
- Lehner, N., Howk, J. C., Tripp, T. M., et al. 2013, *ApJ*, 770, 138, doi: [10.1088/0004-637X/770/2/138](https://doi.org/10.1088/0004-637X/770/2/138)
- Lehner, N., Berek, S. C., Howk, J. C., et al. 2020, *ApJ*, 900, 9, doi: [10.3847/1538-4357/aba49c](https://doi.org/10.3847/1538-4357/aba49c)
- Leung, C., Simha, S., Medlock, I., et al. 2025, arXiv e-prints, arXiv:2507.16816, doi: [10.48550/arXiv.2507.16816](https://doi.org/10.48550/arXiv.2507.16816)
- Li, J.-T., Bregman, J. N., Wang, Q. D., Crain, R. A., & Anderson, M. E. 2018, *ApJL*, 855, L24, doi: [10.3847/2041-8213/aab2af](https://doi.org/10.3847/2041-8213/aab2af)
- Li, S., Riess, A. G., Busch, M. P., et al. 2021, *ApJ*, 920, 84, doi: [10.3847/1538-4357/ac1597](https://doi.org/10.3847/1538-4357/ac1597)
- Lorimer, D. R., Bailes, M., McLaughlin, M. A., Narkevic, D. J., & Crawford, F. 2007, *Science*, 318, 777, doi: [10.1126/science.1147532](https://doi.org/10.1126/science.1147532)
- Macquart, J. P., Prochaska, J. X., McQuinn, M., et al. 2020, *Nature*, 581, 391, doi: [10.1038/s41586-020-2300-2](https://doi.org/10.1038/s41586-020-2300-2)

- Mandigo-Stoba, M. S., Fremling, C., & Kasliwal, M. M. 2022, *Journal of Open Source Software*, 7, 3612, doi: [10.21105/joss.03612](https://doi.org/10.21105/joss.03612)
- Mathews, W. G., & Prochaska, J. X. 2017, *The Astrophysical Journal Letters*, 846, L24, doi: [10.3847/2041-8213/aa8861](https://doi.org/10.3847/2041-8213/aa8861)
- Mohan, N., & Rafferty, D. 2015, *PyBDSF: Python Blob Detection and Source Finder*, *Astrophysics Source Code Library*, record ascl:1502.007
- Nita, G. M., & Gary, D. E. 2010, *Monthly Notices of the Royal Astronomical Society*, 406, L60, doi: [10.1111/j.1745-3933.2010.00882.x](https://doi.org/10.1111/j.1745-3933.2010.00882.x)
- Niu, C. H., Aggarwal, K., Li, D., et al. 2022, *Nature*, 606, 873, doi: [10.1038/s41586-022-04755-5](https://doi.org/10.1038/s41586-022-04755-5)
- Ocker, S. K., Anderson, L. D., Lazio, T. J. W., Cordes, J. M., & Ravi, V. 2024, *ApJ*, 974, 10, doi: [10.3847/1538-4357/ad6a51](https://doi.org/10.3847/1538-4357/ad6a51)
- Oke, J. B., & Gunn, J. E. 1982, *PASP*, 94, 586, doi: [10.1086/131027](https://doi.org/10.1086/131027)
- Oke, J. B., Cohen, J. G., Carr, M., et al. 1995, *PASP*, 107, 375, doi: [10.1086/133562](https://doi.org/10.1086/133562)
- Oppenheimer, B. D., & Schaye, J. 2013, *MNRAS*, 434, 1043, doi: [10.1093/mnras/stt1043](https://doi.org/10.1093/mnras/stt1043)
- Osterbrock, D. E., & Ferland, G. J. 2006, *Astrophysics of gaseous nebulae and active galactic nuclei*
- Perley, D. A. 2019, *Publications of the Astronomical Society of the Pacific*, 131, 084503, doi: [10.1088/1538-3873/ab215d](https://doi.org/10.1088/1538-3873/ab215d)
- Planck Collaboration, Aghanim, N., Akrami, Y., et al. 2020, *A&A*, 641, A6, doi: [10.1051/0004-6361/201833910](https://doi.org/10.1051/0004-6361/201833910)
- Prochaska, J. X., & Zheng, Y. 2019, *MNRAS*, 485, 648, doi: [10.1093/mnras/stz261](https://doi.org/10.1093/mnras/stz261)
- Prochaska, J. X., Macquart, J.-P., McQuinn, M., et al. 2019, *Science*, 366, 231, doi: [10.1126/science.aay0073](https://doi.org/10.1126/science.aay0073)
- Prochaska, J. X., Hennawi, J. F., Westfall, K. B., et al. 2020, *Journal of Open Source Software*, 5, 2308, doi: [10.21105/joss.02308](https://doi.org/10.21105/joss.02308)
- Qu, Z., Huang, R., Bregman, J. N., & Li, J.-T. 2021, *ApJ*, 907, 14, doi: [10.3847/1538-4357/abc9b9](https://doi.org/10.3847/1538-4357/abc9b9)
- Ravi, V., Catha, M., Chen, G., et al. 2023, arXiv e-prints, arXiv:2301.01000, doi: [10.48550/arXiv.2301.01000](https://doi.org/10.48550/arXiv.2301.01000)
- Sánchez-Blázquez, P., Peletier, R. F., Jiménez-Vicente, J., et al. 2006, *MNRAS*, 371, 703, doi: [10.1111/j.1365-2966.2006.10699.x](https://doi.org/10.1111/j.1365-2966.2006.10699.x)
- Shannon, R. M., Bannister, K. W., Bera, A., et al. 2024, arXiv e-prints, arXiv:2408.02083, doi: [10.48550/arXiv.2408.02083](https://doi.org/10.48550/arXiv.2408.02083)
- Sharma, K., Ravi, V., Connor, L., et al. 2024, *Nature*, 635, 61, doi: [10.1038/s41586-024-08074-9](https://doi.org/10.1038/s41586-024-08074-9)
- Simien, F., Athanassoula, E., Pellet, A., et al. 1978, *A&A*, 67, 73
- Spitzer, Lyman, J. 1956, *ApJ*, 124, 20, doi: [10.1086/146200](https://doi.org/10.1086/146200)
- Sunyaev, R. A., & Zeldovich, I. B. 1980, *ARA&A*, 18, 537, doi: [10.1146/annurev.aa.18.090180.002541](https://doi.org/10.1146/annurev.aa.18.090180.002541)
- Thilker, D. A., Braun, R., Walterbos, R. A. M., et al. 2004, *ApJL*, 601, L39, doi: [10.1086/381703](https://doi.org/10.1086/381703)
- Tumlinson, J., Peebles, M. S., & Werk, J. K. 2017, *ARA&A*, 55, 389, doi: [10.1146/annurev-astro-091916-055240](https://doi.org/10.1146/annurev-astro-091916-055240)
- van Leeuwen, J., Kooistra, E., Oostrum, L., et al. 2023, *A&A*, 672, A117, doi: [10.1051/0004-6361/202244107](https://doi.org/10.1051/0004-6361/202244107)
- Westmeier, T., Brüns, C., & Kerp, J. 2008, *MNRAS*, 390, 1691, doi: [10.1111/j.1365-2966.2008.13858.x](https://doi.org/10.1111/j.1365-2966.2008.13858.x)
- Wu, X., & McQuinn, M. 2023, *ApJ*, 945, 87, doi: [10.3847/1538-4357/acbc7d](https://doi.org/10.3847/1538-4357/acbc7d)
- Yao, J. M., Manchester, R. N., & Wang, N. 2017, *ApJ*, 835, 29, doi: [10.3847/1538-4357/835/1/29](https://doi.org/10.3847/1538-4357/835/1/29)
- Zacharie Kam, S., Carignan, C., Chemin, L., et al. 2017, arXiv e-prints, arXiv:1706.04248, doi: [10.48550/arXiv.1706.04248](https://doi.org/10.48550/arXiv.1706.04248)